BNL-207950-2018-JAAM

Using imaging spectroscopy to detect variation in terrestrial ecosystem productivity across a water-stressed landscape

S. DuBois, S. P. Serbin

To be published in "Ecological Applications"

July 2018

Environmental and Climate Sciences Department

Brookhaven National Laboratory

U.S. Department of Energy

USDOE Office of Science (SC), Biological and Environmental Research (BER) (SC-23)

DISCLAIMER

Using imaging spectroscopy to detect variation in terrestrial ecosystem productivity across a water-stressed landscape

Sean DuBois[1,2,3], Ankur R. Desai[3,*], Aditya Singh[2,4], Shawn P. Serbin[5], Michael L. Goulden[6], Dennis D. Baldocchi[7], Siyan Ma[7], Walter C. Oechel[8,9], Sonia Wharton[10], Eric L. Kruger[2], Philip A. Townsend[2]

[1]ICF, Fairfax, VA 22031

[2]University of Wisconsin-Madison, Dept of Forest and Wildlife Ecology, Madison, WI USA

[3]University of Wisconsin-Madison, Dept of Atmospheric and Oceanic Sciences, Madison, WI, USA

[4]University of Florida, Department of Agricultural and Biological Engineering, Gainesville, FL USA

[5]Brookhaven National Laboratory, Environment and Climate Sciences Dept., Upton, NY USA

[6]University of California-Irvine, Dept of Earth System Science, Irvine, CA USA

[7]University of California-Berkeley, Dept. of Environmental Science, Policy, and Management

[8]San Diego State University, Dept. of Biology, San Diego, CA USA

[9]University of Exeter, Dept of Geography, Exeter, UK

[10]Lawrence Livermore National Laboratory, Atmospheric, Earth and Energy Division, Livermore, CA USA

[*]Corresponding author: Ankur R Desai, UW-Madison AOS, AOSS 1549, 1225 W Dayton St, Madison, WI 53706 USA, +1-608-218-4208, desai@aos.wisc.edu

Submitted to: **Ecological Applications (**28 July 2017)

Abstract

A central challenge to understanding how climate anomalies, such as drought and heatwaves, impact the terrestrial carbon cycle, is quantification and scaling of spatial and temporal variation in ecosystem gross primary productivity (GPP). Existing empirical and model-based satellite broadband spectra-based products have been shown to miss critical variation in GPP. Here, we evaluate the potential of high spectral resolution (10 nm) shortwave (400-2500 nm) imagery to better detect spatial and temporal variations in GPP across a range of ecosystems, including forests, grasslands, wetlands, and shrublands in a water-stressed region. Estimates of GPP from eddy covariance (EC) observations were compared against airborne hyperspectral imagery, collected across California during the 2013-2014 HyspIRI airborne preparatory campaign. Observations from 19 flux towers across 23 flight campaigns (102 total image-flux tower pairs) showed GPP to be strongly correlated to a suite of spectral wavelengths and band ratios associated with foliar physiology and chemistry. A partial least squares regression (PLSR) modeling approach was then used to predict GPP with higher validation accuracy [adjusted $R^2 = 0.71$] and low bias (0.04) compared to existing broadband approaches [e.g., adjusted $R^2 = 0.68$ and bias = -5.71 with the Sims *et al.* (2008) model]. Significant wavelengths contributing to the PLSR include those previously shown to coincide with Rubisco (wavelengths 1680, 1740 and 2290 nm) and V_{cmax} (wavelengths 1680, 1722, 1732, 1760, and 2300 nm). These results provide strong evidence that advances in satellite spectral resolution offer significant promise for improved satellite-based monitoring of GPP variability across a diverse range of terrestrial ecosystems.

Keywords: GPP, eddy covariance, imaging spectroscopy, hyperspectral imagery, HyspIRI

Introduction

Recent work by Serbin *et al.* (2015) and Singh *et al.* (2015) has shown promising advancements in the use of hyperspectral imaging, collected from high-altitude airborne missions, to map the variation in the drivers of gross primary productivity (GPP) through measurement of leaf structure, metabolic capacities, and related biochemistry. While the use of broadband spectroscopy on tower, airborne, and satellite platforms to quantify seasonal variation in vegetation greenness, leaf area, and photosynthesis is well established (Carlson and Ripley, 1997; Myneni *et al.*, 2002; Heinsch *et al.*, 2006), imaging spectroscopy affords new opportunities to more accurately monitor spatial and temporal variation in ecosystem function based on its sensitivity to leaf physiology. Imaging spectroscopy (also known as hyperspectral imagery) is here defined as reflectance data consisting of narrowband (5-10 nm) measurements across the full range of visible, near infrared and shortwave infrared wavelengths (VSWIR, 400-2500 nm). Such high-dimensional data take advantage of narrow spectral features related to specific leaf functional, chemical and structural traits (Curran, 1989; Townsend *et al.*, 2016).

In this study, we test an approach using imaging spectroscopy data collected across two years as part of the NASA HyspIRI Preparatory campaign to estimate GPP based on linkage to eddy covariance (EC) data from flux towers, which are currently the most widely used ground data for inferring ecosystem-level GPP. Although data from broadband sensors such as Landsat and MODIS have been used to generate GPP maps across large spatial scales (e.g., Running *et al.*, 2004; Jung *et al.*, 2011), the resulting estimates are subject to large biases and appear to primarily detect broad differences in GPP among ecosystem types and across vegetation density

gradients, potentially missing physiological influences on GPP arising from variations in leaf traits responding to winter dormancy, plant stress, and stomatal response.

For example, the NASA Terra/Aqua-based MODIS GPP MOD17 product correlates well to flux tower GPP estimates, but, on average, monthly GPP overestimates site-level average GPP by 20-30% across a range of land cover types compared to EC, with significant discrepancies between EC and MODIS emerging during phenological transitions (particularly spring green-up) (Heinsch *et al.*, 2006). As well, MODIS GPP did not capture spatial variability observed at the flux tower level between sites of similar vegetation type (Heinsch *et al.*, 2006), especially at the regional scale. As such, a general conclusion is that MODIS may characterize broad variation among physiognomically different ecosystems by detecting differences in vegetation structure and/or cover rather than physiology.

The limits of current broadband remote-sensing techniques to accurately predict spatial or temporal GPP variation (Heinsch *et al.*, 2006) provide an impetus to test the use of imaging spectroscopy to detect variation in vegetation function directly related to GPP. This is motivated by increasing evidence that hyperspectral data are sensitive to biochemical and physiological properties important to ecosystem function (Martin and Aber, 1997; Smith *et al.* 2002; Ollinger and Smith 2005; Asner *et al.*, 2007; Martin *et al.*, 2008; Wolter *et al.*, 2008; Ollinger, 2011; Lee *et al.*, 2015; Schimel *et al.* 2015; Serbin *et al.*, 2015; Singh, 2015; Jetz *et al.*, 2016). For example, high-resolution spectral data have the ability to capture variation in foliar concentrations of water, chlorophyll, cellulose, lignin, nitrogen, and other leaf constituents (Green *et al.*, 1998), and studies have shown the ability to use hyperspectral data to map these and other leaf traits (Ustin and Gamon, 2010; Serbin *et al.*, 2012; Singh *et al.*, 2015).

The NASA HyspIRI Preparatory Airborne mission provided an opportunity to collect a large quantity of high-resolution imagery across a range of EC flux towers in California covering numerous seasons across gradients of vegetation type, density, and physiology of temperate and semi-arid ecosystems with large variation in average GPP. Studied ecosystems ranged from coastal sage and valley grassland systems to high-elevation conifer forests. Our objective was to evaluate the ability of imaging spectroscopy data, through time and across multiple EC flux towers encompassing a range of ecosystem types, to estimate local-scale vegetation productivity. Flux tower measurements were combined with high-spectral and high-spatial resolution narrowband visible to shortwave infrared imaging spectroscopy, repeatedly captured at each tower site with high-altitude airborne sensors, to identify which spectral wavelengths, or combinations of multiple wavelengths (Inoue *et al.*, 2008), relate most strongly to GPP variation within and across sites and compare the use of narrowband (400-2500 nm) spectroscopy data for estimating GPP against existing approaches (e.g., from MODIS) that rely on broadband data.

Methods

GPP estimates using eddy covariance

The EC flux towers span two climate/elevation gradients, a collection of wetland, grassland, and savanna sites in central California, and chaparral/coastal sage sites in southern California (Suppl. Table 1). The latitudinal and topographic gradients create a wide range of mean annual temperature and precipitation among the sites (Suppl. Fig. 1). Further, given the climatological wet season that typically lasts from late autumn to early spring, a number of ecosystem types and plant hydrological adaptations occur in this region, allowing us to observe a wide range of GPP patterns.

Three sets of sites were used here. One climate/elevation gradient crosses the San Jacinto Mountains in southern California, the other ascends from the San Joaquin Valley into the Sierra Nevada Mountains in central California, and the third set includes agricultural and wetland sites (Fig. 1). The southern California gradient includes the following sites (all site names corresponding with the dominant vegetation type): Grassland, Coastal Sage, and Oak-Pine Forest on the western slope of the San Jacinto Mountains, and Pinyon-Juniper Woodland, Desert Chaparral and Sonoran Desert on the eastern slope (Kelly and Goulden, 2008; Goulden *et al.*, 2012), rising from 470 m elevation to 1300 m and back down to 275 m in the desert (Table 1). The Sierra gradient is situated within the Upper Kings River watershed, and comprises grassland-savanna (Oak-Pine Woodland) and forest (Ponderosa Pine and Mixed Conifer) sites (Fig. 1), increasing in elevation from 405 m to 2015 m (Goulden *et al*., 2006).

The wetland and agricultural sites (pasture, rice paddy and alfalfa) are near the San Joaquin River, in the grassland-savanna of the lower Sierra Nevada foothills, and grassland in the Altamont Hills. The wetlands (Twitchell East End Wetland and Mayberry Wetland) are recently restored (2010-2014) and the nearby agricultural fields (Twitchell Island, rice paddy; Twitchell Alfalfa, alfalfa field; Sherman Island, pasture) are actively managed. The sites located in the foothills are located on privately owned land and occasionally grazed by cattle. The Diablo grassland, located in the Altamont Hills, is owned by the Lawrence Livermore National Laboratory and is not actively managed. The southern California shrubland sites are located at the Sky Oaks Field Station (San Diego State University), with one flux tower in old-growth chaparral (Sky Oaks New) and the other in recently naturally burned (2003) chaparral (Sky Oaks Young).

From all 19 tower sites, half-hourly estimates of CO_2 flux were measured using the eddy covariance technique (Aubinet *et al.*, 2011). We gap-filled missing and quality-screened data points using the Desai-Cook gap filling model (Cook *et al.*, 2004; Desai *et al.*, 2005). This model was applied to data filtered according to a turbulence threshold based on friction velocity (u*), utilizing the 30-minute averages for turbulent carbon flux or net ecosystem exchange (NEE). The model uses a variable moving-window mean diurnal variation method to estimate missing meteorological data, with the window size depending on the completeness of the dataset. The Eyring function (Cook *et al.*, 2004) was then applied to the data to estimate ecosystem respiration (R_{eco}). GPP was then estimated as the residual between the 30-minute modeled R_{eco} and the measured NEE data. Variation in the estimated GPP was then related to 30-minute averages for site photosynthetically active radiation (PAR) with a Michaelis-Menton reaction rate equation (Falge *et al.*, 2001). The resulting models afforded GPP predictions when there were NEE gaps in the original dataset, allowing us to adequately characterize seasonal and annual GPP dynamics (Baldocchi *et al.*, 2015). However, comparisons to imagery were limited to periods when NEE observations were measured.

Image acquisition

During the NASA HyspIRI Preparatory Campaign (Hochberg *et al.* 2015, Lee *et al.* 2015), all 19 flux tower sites were repeatedly overflown by the NASA ER-2 aircraft at 20 km, collecting imaging spectroscopy and thermal imagery using the AVIRIS (Airborne Visible/Infrared Imaging Spectrometer) and MASTER (MODIS/Advanced Spaceborne Thermal Emission and Reflection Radiometer Airborne Simulator) sensors (Fig. 1). The AVIRIS sensor measures reflected solar energy in the 380-2510 nm spectral region with 224 spectral bands, with an average bandwidth of 10 nm (Vane *et al.*, 1993, Green *et al.*, 1998). Flights were conducted at

several times throughout the dry and wet seasons and timed to capture maximum variation in plant phenology and ecosystem function (Suppl. Table 2).

The NASA Jet Propulsion Laboratory processed data, including radiometric calibration to surface reflectance following Thompson *et al.* (2015) and ortho-rectification and resampling to consistent 18-m pixels. To normalize between- and within-scene brightness offsets, we performed a brightness correction on all scenes following Feilhauer *et al* (2010) as discussed in Serbin *et al* (2015). Images were topographically corrected using the modified sun-canopy-sensor topographic method (Soenen *et al.* 2005), and cross-track changes in bidirectional reflectance distribution function (BRDF) were corrected using a quadratic function of the volumetric scattering term from the Ross-Thick BRDF model (Roujean *et al.* 1992, Lucht *et al.* 2000). Prior to analysis, we removed the five shortest and longest wavebands, along with those influenced by atmospheric water (1313–1453 nm and 1782–2018 nm), leaving 172 of the 224 channels of AVIRIS data over the 414–2447 nm range.

Image data extraction from tower footprints

For each tower site, AVIRIS data were extracted only from cloud-free acquisitions. Locations of flux towers were identified within AVIRIS images using GPS coordinates, and spectra were extracted only from pixels containing within tower influence areas, as described below. The total number of acquisitions for our analysis was 102, encompassing 19 towers with an average of 5.4 acquisitions from multiple overflights during a 2-year period (Table 1). To identify the vegetation influencing tower GPP, a one-dimensional online footprint model, based on Kljun *et al.* (2015), was used to estimate the size of the tower- influenced footprint at the time of each overflight. The model uses observations or estimates of conditions in the atmospheric

176 boundary layer and canopy layer, including standard deviation of vertical velocity, surface
177 friction velocity, instrument measurement height, boundary layer height, and roughness length.
178 These were derived from the meteorological measurements made at the flux tower or, in the case
179 of boundary layer height, assumed to be 1500 m, for each overflight. Overlapping AVIRIS pixels
180 were based on the upwind distance from the tower so as to encompass 90% of the total surface
181 footprint influence. The footprint crosswind width was calculated as half the total length, so that
182 the footprint was represented as a rectangle beginning from the base of the tower. The 18 m x 18
183 m AVIRIS pixels from this footprint rectangle were then extracted for analysis, with the pixels in
184 the footprint averaged to create a mean reflectance value for each AVIRIS band. The use of the
185 footprint model allows us to address possible bias in flux tower measurements owing to different
186 land cover or photosynthesis rates with direction and distance (Xu *et al*., 2017), a concern
187 particularly at some of the more open and semi-arid sites.

188 ## Linking footprint imagery and tower flux data

189 We adopted two approaches to evaluate the sensitivity of imaging spectroscopy data to
190 variation in GPP. First, we analyzed relationships between GPP and vegetation indices, which
191 are routinely used in remote sensing of vegetation physiology (e.g., Roberts *et al.* 2011). We also
192 statistically modeled GPP variation using partial least squares regression (PLSR) modeling
193 approach, a chemometric method (Wold *et al.* 2001) that is often used for the analysis of
194 hyperspectral imagery (Townsend *et al.* 2003, Martin *et al.* 2008, Wolter *et al.* 2008, Singh *et al.*
195 2015, Serbin *et al.* 2015) because it can exploit the full reflectance spectrum rather than select
196 data subsets (such as vegetation indices) and doesn't assume the remote sensing data were
197 measured without error. Furthermore, PLSR avoids collinearity in the predictor variables (i.e.
198 wavelengths) even when these exceed the number of observations (Geladi and Kowalski, 1986;

199 Wold et al., 2001, Carascal et al., 2009). These issues are avoided by reducing the number of
200 predictor variables down to relatively few, non-correlated latent components, using a stepwise
201 selection method with individual bands or indices (Grossman *et al.* 1996). These latent
202 components capture other nuance in the relationship between the spectra and GPP (e.g. canopy
203 structure, leaf physiology, nutrients) (Asner *et al.* 2008, Asner *et al.* 2011). PLSR is not a
204 standard linear regression, and instead uses singular value decomposition (SVD) to reduce the
205 predictor matrix to a much smaller set of predictor latent components, which are transformed
206 through scores, weightings, and internal relationships to build the vector of regression
207 coefficients by wavelength or index (Geladi and Kowalski, 1986; Wold et al., 2001). This is not
208 a limitation of PLSR but instead a feature of the approach which can allow for the dimensionality
209 reduction of large problems to a much simpler model.

210 For the analysis of vegetation indices, we calculated Normalized Difference Spectral
211 Indices (NDSI) for all combinations of the 172 wavebands in our VSWIR imagery, where, for
212 each pair of bands (e.g., i and j), one band's reflectance value ($Band_j$) is subtracted from the
213 other's ($Band_i$), and the difference is divided by their sum:

$$NDSI[i,j] = [Band_i - Band_j]/[Band_i + Bandj] \qquad \text{(Eq. 1)}$$

214

215 NDSI offers the ability to examine all narrowband features – in this case 14,792 possibilities –
216 and determine their relationship with ecosystem function, such as GPP (Inoue *et al.*, 2008; Ryu
217 *et al.*, 2010). Normalization standardizes NDSI values from -1 to 1 and reduces atmospheric and
218 BRDF effects not otherwise addressed in preprocessing. We note that the NDSI approach
219 includes calculation of several widely used indices, including Normalized Difference Vegetation

220 Index (NDVI, normalized index of 850 and 650 nm, Tucker, 1979) and Photochemical
221 Reflectance Index (PRI, normalized index of 531 and 570 nm, Gamon *et al.* 1992). NDVI is of
222 interest because of its wide use as a correlate with variation in aboveground vegetation structure
223 and greenness, while PRI is related to stress-induced physiological responses (Gamon *et al.*
224 1997, Penuelas *et al.* 1995, Garbulsky *et al.* 2011). There are a vast number of additional
225 multispectral and hyperspectral indices that have been correlated with vegetation function (Ustin
226 *et al.* 2009), but the NDSI approach, covering all possible combinations of bands and their linear
227 combinations, captures the variation expressed in those indices, so the only additional index we
228 tested was a simple chlorophyll index (Gitelson and Merzlyak, 1996), calculated as $[(1/R_{700})$-
229 $(1/R_{850})$-0.1515]/0.01517.

230 We first analyzed correlations between GPP and NDSI using data pooled across all sites,
231 and then performed the same analysis on data subdivided by the four plant functional types
232 (PFTs). Separating data into PFTs enabled assessment of the extent to which correlation was
233 simply a consequence of broad differences in GPP across physiognomic vegetation types that
234 look different in imagery (likely due to differences in physiognomy and/or soil fraction in the
235 AVIRIS pixels), and subsequently whether image spectroscopy could detect variations within
236 types independent of the structural differences among them.

237 PLSR, implemented in Python, was used to examine the relationship between flux tower
238 and imagery data across the full reflectance spectrum, i.e., using all 172 wavebands. Typically,
239 PLSR analyses are applied to reflectance from the 172 bands, enabling the exploitation of all
240 information in the spectrum and resulting in an equation having a beta coefficient for reflectance
241 in each waveband (e.g., Martin *et al.* 2008, Singh *et al.* 2015, Serbin *et al.* 2015). Here, we tested

242 a new approach to PLSR, using the 14,792 NDSI combinations rather than reflectance bands as
243 inputs. The closest 30 minute average GPP estimate to image acquisition was used to minimize
244 the effects of diurnal changes in productivity. We performed 1,000 permutations of the data with
245 a 2/3-1/3 split for calibration and validation. We determined the number of components to be
246 used for model fitting by successively increasing the number of components from 1 to 15 till
247 model validation statistics indicated overfitting. Once the number of components had been fixed,
248 we extracted 2/3 of the data using a stratified random sampling strategy based on the land cover,
249 and applied the model to the 1/3 of the withheld data for validation. In addition, to reflect
250 uncertainties in the response variable, we added noise equivalent to 20% of each observation
251 during each iteration by sampling from a normal distribution with a mean at the observation, and
252 a standard deviation equal to 20% of the mean. This way, our modeling strategy accounts for
253 uncertainties in data completeness by randomly dropping 1/3 of the tower sites, and in addition,
254 accounts for uncertainties in the observations themselves. At each model iteration, we stored the
255 PLSR coefficients, and present calibration and validation R^2, biases, and RMSEs as a percent of
256 variation as model diagnostics. Supplemental Table 4 shows overall model performance
257 diagnostics, and diagnostics averaged across functional types. A heat graph of model coefficients
258 by wavelength pairs was used to illustrate the importance of specific wavelengths and
259 wavelength combinations as predictors of flux tower GPP from AVIRIS data. Use of NDSI
260 rather than reflectance enables us to test whether identification of narrow absorption features is
261 more predictive of vegetation function than magnitude of reflectance at a particular wavelength.

262 Lastly, we compared the predictive capacity of imaging spectroscopy from high-altitude
263 AVIRIS against standard methods used to estimate GPP from broadband measurements. For this,
264 we applied the broadband light-use efficiency method of Sims *et al.* (2008) to estimate satellite-

265 derived GPP using Terra MODIS broadband-based enhanced vegetation index (EVI) and land
266 surface temperature (LST), which has previously been shown to outperform the traditional and
267 similar MOD17 GPP product by including a scalar to account for a water stress response of GPP
268 (Sims *et al.*, 2008). For the comparison, we convolved the AVIRIS wavelengths corresponding
269 with the MODIS bands used to calculate EVI. We used LST estimates from the MODIS/ASTER
270 airborne simulator (MASTER) (Hook *et al.*, 2001), which was acquired simultaneously with
271 AVIRIS imagery (Lee *et al.* 2015). Sims *et al.* (2008) parameterized the scalar quantity *m* using
272 three years of flux tower data. The model developed in Sims *et al.* (2008) requires mean annual
273 nighttime LST estimates in the calibration of parameter *m*. However, there were not enough
274 MASTER flights conducted at night to make this approach viable, so we instead used the mean
275 of annual nighttime temperature calculated from flux tower data. Finally, we also compared the
276 MODIS GPP product to tower GPP using the 1-km MODIS pixel encompassing the tower
277 location (LP DAAC, 2015). Tower GPP was then aggregated to 8-day estimates to match the
278 MODIS product.

279 ## Results

280 The two-year study period occurred during a period of lower than average precipitation
281 and higher than average temperature (Table 1, Suppl. Fig. 1). Over this time, among our 19
282 tower sites, the desert site recorded the lowest daily average tower-based GPP, 0.5 μmol m^{-2} s^{-1},
283 while the irrigated Twitchell Alfalfa site (USTW3), which becomes highly productive between
284 cuttings, set the maximum, 25.6 μmol m^{-2} s^{-1} (Fig. 2). The coefficient of variation for GPP (30-
285 minute average) at the time of AVIRIS overflights was 70% within individual tower sites, and
286 109% averaged across sites.

287 Heat graphs (Figs. 3-4) illustrate correlations between GPP (30-minute average) at the
288 time of overflight and NDSI calculated for each of the 14,792 waveband combinations in the
289 corresponding footprint hyperspectral imagery. GPP and NDSI were closely correlated ($|r| > 0.6$)
290 in broad regions of the spectrum when data were pooled across all sites (Fig. 3). In contrast,
291 within vegetation types, strong correlations were generally restricted to narrower regions of the
292 spectrum. Particular bands of high correlation include 414-434 nm, 704-714 nm, and 743-792
293 nm (Suppl. Table 3). In forests (Fig. 4a), high correlation ($|r| > 0.7$) occurred only when NDSI
294 was generated from two groups of narrowband wavelength combinations, one based on 890-909
295 nm with 812 nm and another with 2278-2307 nm against 2138-2198 nm, reflective of larger
296 differences in near infrared albedo across forest types and changes in shortwave infrared related
297 to canopy structure, water content, and leaf nitrogen. Among the widely used vegetation indices
298 that we evaluated, NDVI and the chlorophyll index correlated with GPP ($R^2 = 0.70$ and 0.44
299 respectively) across all sites (Fig. 3), but these relationships were not significant within the forest
300 type (Fig. 4, $p>0.05$). PRI, on the other hand, did not correlate with GPP across sites ($p>0.05$).

301 PLSR results reveal high fidelity in the ability to predict GPP across all sites and
302 vegetation types ($R^2 = 0.78$, $P < 0.0001$, Fig. 5a), with all cover types performing similarly. The
303 only significant difference between slopes of actual vs. predicted GPP occurred between
304 grasslands and forest ($P = 0.0015$). Normalized PLSR coefficients (Fig. 6) indicate that an array
305 of specific features, distributed throughout the entire spectrum, contribute substantively to the
306 predictive model. Important narrow spectral regions in the predictive model included NDSI band
307 combinations using 1250-1280 nm (combined in particular with wavelengths across the NIR),
308 2030-2050 nm, and 2270-2300 nm. Broader SWIR features important to the model incudes

NDSIs in the 1710-1780 nm (when combined with 1250-1270 nm) and 1500-1680 nm regions (Fig. 6).

In contrast, the Sims broadband approach for remote estimation of GPP from spectra (Fig. 5b) is generally able to differentiate highest from lowest values of GPP across all types (R^2 = 0.68, P < 0.0001), but not as well as the PLSR approach, and does not accurately predict spatial and temporal variation in GPP within functional types. Slopes between actual and predicted GPP (Fig. 5b) vary significantly between grassland and forest (P = 0.0044), grasslands and shrublands (P = 0.041), and grasslands and wetlands (P = 0.0041). The models also deviate considerably from the 1:1 line compared the PLSR approach. This outcome is also replicated using other approaches such as the MODIS GPP product (MOD17A2.005) (Suppl. Fig. 2).

Discussion

Water stress is likely one of the strongest drivers of large-scale GPP reductions globally (Ciais *et al.*, 2003). Collectively, the results of this study illustrate the capacity of imaging spectroscopy to more accurately capture spatial and temporal variation in terrestrial ecosystem GPP over a water-stressed landscape, though additional years of observations over the same sites in non-drought conditions would be required to evaluate the full capability of the approach. In addition to its improved predictive capability relative to existing remote sensing approaches, an appealing advantage of the narrowband PLSR model we derived, relative to conventional broadband approaches, is that it does not require external inputs of meteorology or parameters related to plant ecophysiology.

Although the potential of imaging spectroscopy to track GPP has been shown at individual towers (Matthes *et al.*, 2015; Gamon *et al.*, 2015) and with individual indices (Alton, 2017), our study is the first to demonstrate the capability across a diverse array of ecosystems, utilizing the full information content of narrowband spectra. Our results provide a robust initial assessment of the reliability of spatial extrapolation from hyperspectral imagery to justify the benefits of proposed future missions to GPP mapping (Schimel *et al.* 2015).

It is likely that a significant improvement in the fit over broadband occurs primarily from directly capturing the effects of physiology on GPP, which are highly variable over space and time. This improvement may be most noticeable in evergreen species, whose leaf phenology and density may be relatively constant, limiting broadband sensitivity to GPP variation. While a direct PLSR approach was not applied to the MODIS bands separately, the Sims model tested here represents the best-in-class for currently published MODIS based GPP algorithms. There are limitations in the comparison with the Sims model, as we were required to use air temperature rather than LST for the nighttime temperature measurements. However, modest adjustments in nighttime temperature parameters are unlikely to change the conclusion the PLSR model outperformed the broadband based model.

High correlations occurring with NDSIs at using wavelengths close to each other in the spectra indicate the importance of narrow features in the spectrum to vegetation properties that influence tower GPP. The heat graph of NDSI contributions to the PLSR model of GPP (Fig. 6) indicates several key narrowband combinations that are important to predicting tower GPP, especially in wavelength regions that have been shown to be important to vegetation physiology. Our findings mirror those of previous studies (e.g. Matthes *et al.*, 2015; Zarco-Tejada *et al.*,

2001; Singh *et al.*, 2015; Ryu *et al.,* 2010), which show a number of consistent regions of high correlation between GPP and narrowband NDSI. Ryu *et al.* (2010) used NDSI to compare spectra in the range of 400 nm and 900 nm with assimilation calculated using a similar flux partitioning method at the Vaira Ranch site between 2006 and 2009. The wavelength combinations associated with high and low correlation in the NDSI figure from the Ryu *et al.* (2010) study match the NDSI figure from this study for the Grassland group of sites, which includes the Vaira Ranch site. The broad areas of high correlation for the given spectral range are present in both figures, as are the narrow features of low correlation associated with indices involving 700 nm and the range 400 to 700 nm, and 750 nm and the range 750 to 900 nm. Unlike Ryu et al, we were also able to demonstrate consistently important wavelengths in the shortwave infrared (SWIR, >1100 nm).

Our findings confirm that specific features are associated with leaf/canopy spectral traits that reflect variation in leaf structure and function. The wavelengths significant to our PLSR model coincide with important physiological features, which is consistent with previous analyses showing AVIRIS wavelengths can be used to predict photosynthetic capacity via known features as opposed to simply measuring canopy structure (Serbin *et al.,* 2015). Narrow NDSI combinations of wavelengths in the SWIR (2050 nm) and near infrared (760 nm) appear especially influential, as do some broader features around 1200, 1600 and 2200 nm. For the shortwave infrared regions, RuBisCo has known spectral absorption features around wavelengths 1500, 1680, 1740, 2050, and 2290 (also: 1940, 2170 and 2470 nm) (Elvidge, 1990), while significant wavelengths in the leaf-level V_{cmax} model presented in Serbin *et al.* (2012) occur at 1510, 1680 and 1760, nm (also 1940, 2210, and 2490 nm). Using AVIRIS imagery, Serbin *et al.* (2015) identified key features at 1158-1168, 1722-1732 and 2300-2400 nm.

In contrast, across all sites, the visible and near infrared regions (VNIR, 400-1100 nm) did not exhibit as many key features for predicting GPP as did the SWIR. However, key narrow features do appear in the chlorophyll a absorption wavelengths at 414-434 nm, the red-edge (704-714 nm), and in the NIR (743-792 nm, including 763 nm, near a well-documented chlorophyll fluorescence feature). Spectral features such as the broader red edge (690-750 nm) are unsurprising as they are known to shift under water stress conditions (Vogelmann *et al.*, 1993), one of the major contributors to variations in GPP in the ecosystems of California that were strongly affected by drought during our study period (Asner *et al.*, 2016). These findings demonstrate that the improved predictive performance of a model based on imaging spectroscopy likely results from exploiting multiple mechanistic links among observed plant pigments, traits, and functional response.

Using the NDSIs (rather than raw reflectance wavelengths) allows the identification of combinations of narrow features (one or two wavebands wide) that appear repeatedly as important in our model. The heat graph for the PLSR coefficients using NDSI show a range of narrow features with high contribution to the PLSR (e.g., 2288 nm) and wider features indicating broader correlations, likely related to vegetation water content (e.g., 1503-1682 nm). In particular, combinations of narrow wavebands centered on 414, 1762, 2048 and 2298 appeared repeatedly in the PLSR model (indicated by streaks in the heat graph in Fig. 6). The value to PLSR used in the way presented here is that we were able to exploit both the full spectrum in the PLSR, but also narrow features at specific wavebands that emerged in the important NDSIs in the model.

The differences between the correlation heat maps (Figs. 3 and 4) and PLSR heatmap (Fig. 6) demonstrate the value of the imaging spectroscopy and PLSR approaches in estimating GPP across broadly varying ecosystems. Simple correlations with NDSI in which all cover types are pooled (Fig. 3) indicate that broad areas of the spectrum characterized by widely used indices such as NDVI, rather than narrow features that require imaging spectroscopy, are sufficient to capture major variation in GPP that is largely attributable to differences in physiognomic cover type (e.g., forest vs. grassland). This suggests decent discrimination of differences between types but poor predictability within types (Fig 5b).

In contrast, the correlation heat graph broken out by cover type (Fig. 4) shows widely differing correlations between GPP and hyperspectral NDSIs by type, and indicates that both narrow and broad regions within different cover types are important correlates with GPP. Moving to a predictive framework, the PLSR of all data using NDSIs (Figs 5a, 6) demonstrates that the imaging spectroscopy data – using NDSIs – can effectively discriminate variations in GPP encompassing differences between and within cover types. When contrasted with broadband approaches (5a vs. 5b), both imaging spectroscopy and broadband analyses adequately capture variations associated with type differences, although the imaging spectroscopy model exhibits less bias (Fig 5a) than the broadband model (Fig 5b), with the imaging spectroscopy PLSR approach standing out in that the different cover types more closely align along the same 1:1 line than the broadband approach. The limited dataset does not allow in depth analysis of model performance for each vegetation type, but the model generated more accurate predicted GPP for Grassland-Savanna, Shrubland and Wetland, while the Forest type exhibited the lowest correlation (Suppl. Table 4). The NDSI values associated with the Forest set of sites also exhibited the lowest overall average correlation (Fig. 4). The lower relative

418 performance of both the model and average NDSI correlation for Forest sites compared to the
419 other types is expected, as the LAI for these sites is relatively constant throughout the growing
420 season, as compared to other sites with a less dense canopy. Broad spectral areas of correlation
421 (Fig. 4) are prevalent in sites where LAI is highly correlated with ecosystem productivity. For
422 this reason, broadband-based productivity models can generally perform well across vegetative
423 types, while the relationship breaks down within a classification (Fig. 5b). Furthermore, variation
424 within a single site has been difficult to detect with all existing models examined, but the
425 narrowband-based model presented in this study is able to maintain low error and bias within
426 vegetation types, including Forest sites which produced the lowest adjusted R^2 value (0.32). The
427 result of this ability to capture variability within PFTs is a more robust model when compared to
428 broadband based predictive models including the Sims model (Fig. 5). We provide the first
429 evidence that a complex range of sites can be well simulated with no additional information
430 beyond the spectral content and the PLSR model. Additional research and sampling is required
431 to examine potential methods to improve predictability within Forest sites.

432 Collectively, these analyses enable us to determine the capacity to extrapolate ecosystem
433 function derived from flux tower data using hyperspectral imagery, and then infer ecosystem
434 responses to climate anomalies such as the unprecedented drought that occurred in California
435 during our study period (Asner *et al.,* 2016). Challenges remain in handling diverse canopy
436 architecture, especially open canopies with large soil exposed gaps, and integrating across
437 complex terrain, land management, and seasonally stressed ecosystems (Kobayashi *et al.*, 2012).
438 Additional measurements across a wider range of climatic and ecological conditions will be
439 required to develop a useful model at broader scales. Nonetheless, our findings have an

important bearing on proposed future satellite-borne imaging spectroscopy missions that could fill the gaps in the globally sparse network of EC flux towers (Schimel *et al.* 2015).

Conclusion

Flux tower estimates of GPP across multiple ecosystems in a water-stressed region offer important observations that can inform remote sensing algorithm development for improved detection of drought impacts on carbon cycling and plant productivity. PLSR models based on imaging spectroscopy with high spectral resolution are capable of accurately predicting GPP independent of vegetation type and season, with significant improvement over traditional broadband approaches. Use of NDSIs in our PLSR models enabled us to leverage not only the full spectrum, as is common with hyperspectral imagery, but also narrow features identifiable in combinations of narrow bands, which has not typically been done in hyperspectral analyses, as usually just reflectance by wavelength is used.

Our findings provide the opportunity to accurately map ecosystem properties where broadband sensor capabilities are limited and suggest that spectral resolution is as or even more important than spatial resolution in consideration of future sensor design for satellite remote sensing. Further, there is strong evidence for mechanistic links among wavelengths and response associated with specific elements in leaf structure that influence plant productivity, and therefore GPP, on a canopy scale. We conclude that the sensitivity of ecosystem metabolism to ongoing and future climatic changes can be monitored continuously at high spatial resolution using satellites equipped with sensors similar to the proposed HyspIRI imaging spectrometer.

Acknowledgments

SD, ARD, AS, SS, EK, and PT acknowledge support for this project by a NASA HyspIRI Preparatory Project award #NNX12AQ28G made to U. Wisconsin. Support for eddy covariance flux tower measurements and databases comes from the Department of Energy Office of Science Ameriflux Network Management Project. SS was supported by the United States Department of Energy contract No. DE-SC0012704 to Brookhaven National Laboratory in the writing of this manuscript. Flux tower data are available from the DOE Ameriflux database (http://ameriflux.lbl.gov/) or by direct contact to the PI. HyspIRI airborne imagery is available from the NASA AVIRIS data portal. PLSR model results are available at the EcoSIS repository (https://ecosis.org/). The authors thank Andrew Jablonski for assistance with image processing.

Works Cited

Alton, P.B. (2017). Retrieval of seasonal Rubisco-limited photosynthetic capacity at global FLUXNET sites from hyperspectral satellite remote sensing: Impact on carbon modeling. *Agricultural and Forest Meteorology*, 232, 74-88, doi:10.1016/j.agrformet.2016.08.001

Asner, G.P., Knapp, D.E., Kennedy-Bowdin, T., Jones, M.O., Martin, R.E., Boardman, J.W., & Field, C.B. (2007). Carnegie Airborne Observatory: in-flight fusion of hyperspectral imaging and waveform light detection and ranging for three-dimensional studies of ecosystems. *J Applied Remote Sensing*, 1, 013536, doi:10.1117/1.2794018

Asner, G. P., & Martin, R. E. (2008). Spectral and chemical analysis of tropical forests: Scaling from leaf to canopy levels. *Remote Sensing of Environment,* 112, 3958-3970

Asner, G. P., Martin, R. E., Knapp, D. E., Tupayachi, R., Anderson, C., Carranza, L., Martinez, P., Houcheime, M., Sinca, F., & Weiss, P. (2011). Spectroscopy of canopy chemicals in humid tropical forests. *Remote Sensing of Environment, 115*, 3587-3598

Asner, G.P., Brodrick, P.G., Anderson, C.B., Vaughn, N., Knapp, D.E., & Martin, R.E. (2016). Progressive forest canopy water loss during the 2012-2015 California drought. *Proceedings of the National Academy of Sciences of the United States of America, 113*, E249-E255

Aubinet, M., Vesala, T., Papale, D., eds., *Eddy Covariance: A Practical Guide to Measurement and Data Analysis*. Berlin, Germany: Spring Atmospheric Sciences, ISBN: 978-94-007-2350-4, 438 pages, pp. 263-289, doi:10.1007/978-94-007-2351-1_9

Baldocchi, D., C. Sturtevant, and C. Fluxnet (2015). Does day and night sampling reduce spurious correlation between canopy photosynthesis and ecosystem respiration? *Agricultural and Forest Meteorology* 207,117-126

Carlson, T.N., & Ripley, D.A. (1997). On the relation between NDVI, fractional vegetation cover, and leaf area index. *Rem. Sens. Environ.* 62, 241-252.doi: 10.1016/S0034-4257(97)00104-1

Carrascal, L. M., Galván, I., & Gordo, O. (2009). Partial least squares regression as an alternative to current regression methods used in ecology. *Oikos, 118*, 681-690

Ciais, P., Reichstein, M., Viovy, N., Granier, A., Ogee, J., Allard, V., Aubinet, M., Buchmann, N., Bernhofer, C., Carrara, A., Chevallier, F., De Noblet, N., Friend, A.D., Friedlingstein, P., Grunwald, T., Heinesch, B., Keronen, P., Knohl, A., Krinner, G., Loustau, D., Manca, G., Matteucci, G., Miglietta, F., Ourcival, J.M., Papale, D., Pilegaard, K., Rambal, S., Seufert, G., Soussana, J.F., Sanz, M.J., Schulze, E.D., Vesala, T., & Valentini, R. (2005). Europe-wide reduction in primary productivity caused by the heat and drought in 2003. *Nature, 437*, 529-533

Cook, B.D., Davis, K.J., Wang, W.G., Desai, A., Berger, B.W., Teclaw, R.M., Martin, J.G., Bolstad, P.V., Bakwin, P.S., Yi, C.X., & Heilman, W. (2004). Carbon exchange and venting anomalies in an upland deciduous forest in northern Wisconsin, USA. *Agricultural and Forest Meteorology, 126*, 271-295

Curran, P.J. (1989) Remote Sensing of Foliar Chemistry. *Remote Sensing of the Environment*, *30,* 271-278

Desai, A.R., Bolstad, P.V., Cook, B.D., Davis, K.J., & Carey, E.V. (2005). Comparing net ecosystem exchange of carbon dioxide between an old-growth and mature forest in the upper Midwest, USA. *Agricultural and Forest Meteorology, 128*, 33-55

Desai, A.R., Richardson, A.D., Moffat, A.M., Kattge, J., Hollinger, D.Y., Barr, A., Falge, E., Noormets, A., Papale, D., Reichstein, M., and Stauch, V.J. (2008). Cross site evaluation of eddy covariance GPP and RE decomposition techniques. *Agricultural and Forest Meteorology*, *148*(6-7)*,* 821-838

Elvidge, C.D. (1990). Visible and near-infrared reflectance characteristics of dry plant materials. *International Journal of Remote Sensing, 11*, 1775-1795

Falge, E., Baldocchi, D., Olson, R., Anthoni, P., Aubinet, M., Bernhofer, C., Burba, G., Ceulemans, R., Clement, R., Dolman, H., Granier, A., Gross, P., Grunwald, T., Hollinger, D., Jensen, N.O., Katul, G., Keronen, P., Kowalski, A., Lai, C.T., Law, B.E., Meyers, T., Moncrieff, H., Moors, E., Munger, J.W., Pilegaard, K., Rannik, U., Rebmann, C., Suyker, A., Tenhunen, J., Tu, K., Verma, S., Vesala, T., Wilson, K., & Wofsy, S. (2001). Gap filling strategies for defensible annual sums of net ecosystem exchange. *Agricultural and Forest Meteorology, 107*, 43-69

Feilhauer, H., Asner, G.P., Martin, R.E., & Schmidtlein, S. (2010). Brightness-normalized Partial Least Squares Regression for hyperspectral data. *Journal of Quantitative Spectroscopy & Radiative Transfer, 111*, 1947-1957

Gamon, J. A., Penuelas, J., & Field, C. B. (1992). A narrow-waveband spectral index that tracks diurnal changes in photosynthetic efficiency. *Remote Sensing of environment*, *41*(1), 35-44

Gamon, J.A., Serrano, L., & Surfus, J.S. (1997). The photochemical reflectance index: an optical indicator of photosynthetic radiation use efficiency across species, functional types, and nutrient levels. *Oecologia, 112*, 492-501

536 Gamon, J.A. (2015). Reviews and Syntheses: optical sampling of the flux tower
537 footprint. *Biogeosciences, 12*, 4509-4523
538 Garbulsky, M. F., Peñuelas, J., Gamon, J., Inoue, Y., & Filella, I. (2011). The photochemical
539 reflectance index (PRI) and the remote sensing of leaf, canopy and ecosystem radiation
540 use efficiencies: A review and meta-analysis. *Remote Sensing of Environment*, *115*(2),
541 281-297
542 Geladi, P., & Kowalski, B.R. (1986). Partial least-squares regression - A tutorial. *Analytica*
543 *Chimica Acta 185,* 1-17
544 Gittelson, A.A., & Merzlyak, M. (1996). Signature Analysis of Leaf Reflectance Spectra:
545 Algorithm Development for Remote Sensing of Chlorophyll. *J. Plant Physiology*, *148*,
546 494-500
547 Goulden, M.L., Winston, G.C., McMillan, A.M.S., Litvak, M.E., Read, E.L., Rocha, A.V., &
548 Elliot, J.R. (2006). An eddy covariance mesonet to measure the effect of forest age on
549 land-atmosphere exchange. *Global Change Biology, 12*, 2146-2162
550 Goulden, M.L., Anderson, R.G., Bales, R.C., Kelly, A.E., Meadows, M., & Winston, G.C.
551 (2012). Evapotranspiration along an elevation gradient in California's Sierra
552 Nevada. *Journal of Geophysical Research-Biogeosciences, 117*, G03028,
553 doi:10.1029/2012JG002027
554 Green, R.O., Eastwood, M.L., Sarture, C.M., Chrien, T.G., Aronsson, M., Chippendale, B.J.,
555 Faust, J.A., Pavri, B.E., Chovit, C.J., Solis, M.S., Olah, M.R., & Williams, O. (1998).
556 Imaging spectroscopy and the Airborne Visible Infrared Imaging Spectrometer
557 (AVIRIS). *Remote Sensing of Environment, 65*, 227-248
558 Grossman Y.L., Ustin S.L., Jacquemoud S., Sanderson E.W., Schmuck G., & Verdebout J.
559 (1996) Critique of stepwise multiple linear regression for the extraction of leaf
560 biochemistry information from leaf reflectance data. *Remote Sensing of Environment* 56,
561 182–193.
562 Heinsch, F.A., Zhao, M.S., Running, S.W., Kimball, J.S., Nemani, R.R., Davis, K.J., Bolstad,
563 P.V., Cook, B.D., Desai, A.R., Ricciuto, D.M., Law, B.E., Oechel, W.C., Kwon, H., Luo,
564 H.Y., Wofsy, S.C., Dunn, A.L., Munger, J.W., Baldocchi, D.D., Xu, L.K., Hollinger,
565 D.Y., Richardson, A.D., Stoy, P.C., Siqueira, M.B.S., Monson, R.K., Burns, S.P., &
566 Flanagan, L.B. (2006). Evaluation of remote sensing based terrestrial productivity from
567 MODIS using regional tower eddy flux network observations. *Ieee Transactions on*
568 *Geoscience and Remote Sensing, 44*, 1908-1925
569 Hochberg, E.J., Roberts, D.A., Dennison, P.E., & Hulley, G.C. (2015). Special issue on the
570 Hyperspectral Infrared Imager (HyspIRI): Emerging science in terrestrial and aquatic
571 ecology, radiation balance and hazards. *Rem. Sens. Enviorn.* 167, 1-5, doi:
572 10.1016/j.rse.2015.06.011
573 Hook, S.J., Myers, J.E.J., Thome, K.J., Fitzgerald, M., & Kahle, A.B. (2001). The
574 MODIS/ASTER airborne simulator (MASTER) - a new instrument for earth science
575 studies. *Remote Sensing of Environment, 76*, 93-102
576 Inoue, Y., Penuelas, J., Miyata, A., & Mano, M. (2008). Normalized difference spectral indices
577 for estimating photosynthetic efficiency and capacity at a canopy scale derived from
578 hyperspectral and CO2 flux measurements in rice. *Remote Sensing of Environment, 112*,
579 156-172
580 Jetz, W., *et al.* (2015). Monitoring plant functional diversity from space. *Nature Plants*, 2,
581 16024, doi: 10.1038/NPLANTS.2016.24.

582 Jung M., et al. (2011), Global patterns of land-atmosphere fluxes of carbon dioxide, latent heat,
583 and sensible heat derived from eddy covariance, satellite, and meteorological
584 observations, *J. Geophys. Res.*, 116, G00J07, doi:10.1029/2010JG001566
585 Kelly, A.E., & Goulden, M.L. (2008). Rapid shifts in plant distribution with recent climate
586 change. *Proceedings of the National Academy of Sciences of the United States of*
587 *America, 105*, 11823-11826
588 Kljun, N., Calanca, P., Rotach, M. W., and Schmid, H. P. (2015) A simple two-dimensional
589 parameterisation for Flux Footprint Prediction (FFP), Geosci. Model Dev., 8, 3695-3713,
590 doi:10.5194/gmd-8-3695-2015.
591 Kobayashi, H., Baldocchi, D.D. Ryu, Y. Chen, Q., Ma, S., Osuna, J.L., & Ustin, S.L. (2012)
592 Modeling energy and carbon fluxes in a heterogeneous oak woodland: A three-
593 dimensional approach. *Agricultural and Forest Meteorology,* 152, 83-100.
594 Land Processes Distributed Active Archive Center (LP DAAC) (2001) MODIS GPP
595 (MOD17A2.005). NASA EOSDIS Land Processes DAAC, USGS Earth Resources
596 Observation and Science (EROS) Center, Sioux Falls, South Dakota
597 (https://lpdaac.usgs.gov), accessed October 22, 2015, at
598 https://lpdaacsvc.cr.usgs.gov/appeears
599 Lee, C.M., Cable, M.L., Hook, S.J., Green, R.O., Ustin, S.L., Mandl, D.J., and Middleton, E.M.
600 (2015). An introduction to the NASA Hyperspectral InfraRed Imager (HyspIRI) mission
601 and preparatory activities. *Remote Sensing of Environment*, *167*, 6-19,
602 doi:10.1016/j.rse.2015.06.012.
603 Lucht, W., Schaaf, C.B., & Strahler, A.H. (2000). An algorithm for the retrieval of albedo from
604 space using semiempirical BRDF models. *Ieee Transactions on Geoscience and Remote*
605 *Sensing, 38*, 977-998
606 Martin, M.E., & Aber, J.D (1997) High Spectral Resolution Remote Sensing of Forest Canopy
607 Lignin, Nitrogen, and Ecosystem Processes. *Ecological Applications*, 7, 431-443.
608 Martin, M.E., Plourde, L.C., Ollinger, S.V., Smith, M.L., & McNeil, B.E. (2008) A generalizable
609 method for remote sensing of canopy nitrogen across a wide range of forest
610 ecosystems. *Remote Sensing of Environment, 112*, 3511-3519
611 Matthes, J.H., Knox, S.H., Sturtevant, C., Sonnentag, O., Verfaillie, J., & Baldocchi, D. (2015)
612 Predicting landscape-scale CO2 flux at a pasture and rice paddy with long-term
613 hyperspectral canopy reflectance measurements. *Biogeosciences, 12*, 4577-4594
614 Myneni, R.B., et al. (2002) Global products of vegetation leaf area and fraction absorbed PAR
615 from year one of MODIS data. *Remote Sensing Environment* 83, 214-231,
616 doi:10.1016/S0034-4257(02)00074-3
617 Ollinger, S.V., & Smith, M.L. (2005) Net primary production and canopy nitrogen in a temperate
618 forest landscape: An analysis using imaging spectroscopy, modeling and field
619 data. *Ecosystems, 8*, 760-778
620 Ollinger, S.V. (2011) Sources of variability in canopy reflectance and the convergent properties
621 of plants. *New Phytologist*, 189, 375–394, doi:10.1111/j.1469-8137.2010.03536.x
622 Penuelas, J., Filella, I., & Gamon, J. A. (1995) Assessment of photosynthetic radiation-use
623 efficiency with spectral reflectance. *New Phytologist*, *131*(3), 291-296
624 Roberts, DA, KL Roth and RL Perroy, Hyperspectral Vegetation Indices, pp 309-327 in PS
625 Thenkabail, JG Lyon and A Huete Hyperspectral Remote Sensing of Vegetation, CRC
626 Press 2011

627 Roujean, J.L., Leroy, M., & Deschamps, P.Y. (1992). A BIDIRECTIONAL REFLECTANCE
628 MODEL OF THE EARTHS SURFACE FOR THE CORRECTION OF REMOTE-
629 SENSING DATA. *Journal of Geophysical Research-Atmospheres, 97*, 20455-20468
630 Ryu, Y., Baldocchi, D.D., Verfaillie, J., Ma, S., Falk, M., Ruiz-Mercado, I., Hehn, T., &
631 Sonnentag, O. (2010) Testing the performance of a novel spectral reflectance sensor,
632 built with light emitting diodes (LEDs), to monitor ecosystem metabolism, structure and
633 function. *Agricultural and Forest Meteorology, 150*, 1597-1606
634 Running, S.W., Nemani, R.R., Heinsch, F.A., Zhao, M., Reeves, M., & Hashimoto, H. (2004) A
635 Continuous Satellite-Derived Measure of Global Terrestrial Primary Production.
636 *BioScience* 54, 547-560, doi: 10.1641/0006-3568(2004)054[0547:ACSMOG]2.0.CO;2
637 Schimel, D., Pavlick, R., Fisher, J. B., Asner, G. P., Saatchi, S., Townsend, P., Miller, C.,
638 Frankenberg, C., Hibbard, K. and Cox, P. (2015) Observing terrestrial ecosystems and
639 the carbon cycle from space. *Glob Change Biol*, 21: 1762–1776. doi:10.1111/gcb.12822
640 Serbin, S.P., Dillaway, D.N., Kruger, E.L., & Townsend, P.A. (2012) Leaf optical properties
641 reflect variation in photosynthetic metabolism and its sensitivity to temperature. *Journal*
642 *of Experimental Botany, 63*, 489-502
643 Serbin, S.P., Singh, A., Desai, A.R., DuBois, S.G., Jablonsld, A.D., Kingdon, C.C., Kruger, E.L.,
644 & Townsend, P.A. (2015). Remotely estimating photosynthetic capacity, and its response
645 to temperature, in vegetation canopies using imaging spectroscopy. *Remote Sensing of*
646 *Environment, 167*, 78-87
647 Sims, D.A., Rahman, A.F., Cordova, V.D., El-Masri, B.Z., Baldocchi, D.D., Bolstad, P.V.,
648 Flanagan, L.B., Goldstein, A.H., Hollinger, D.Y., Misson, L., Monson, R.K., Oechel,
649 W.C., Schmid, H.P., Wofsy, S.C., & Xu, L. (2008) A new model of gross primary
650 productivity for North American ecosystems based solely on the enhanced vegetation
651 index and land surface temperature from MODIS. *Remote Sensing of Environment, 112*,
652 1633-1646
653 Singh, A., Serbin, S.P., McNeil, B.E., Kingdon, C.C., & Townsend, P.A. (2015) Imaging
654 spectroscopy algorithms for mapping canopy foliar chemical and morphological traits
655 and their uncertainties. *Ecological Applications, 25*, 2180-2197
656 Smith, M.-L., Ollinger, S. V., Martin, M. E., Aber, J. D., Hallett, R. A. and Goodale, C. L.
657 (2002) Direct estimation of aboveground forest productivity through hyperspectral
658 remote sensing of canopy nitrogen. *Ecological Applications*, 12, 1286–1302,
659 doi:10.1890/1051-0761(2002)012[1286:DEOAFP]2.0.CO;2
660 Soenen, S.A., Peddle, D.R., & Coburn, C.A. (2005) SCS+C: A modified sun-canopy-sensor
661 topographic correction in forested terrain. *Ieee Transactions on Geoscience and Remote*
662 *Sensing, 43*, 2148-2159
663 Thompson, D.R., Gao, B.C., Green, R.O., Roberts, D.A., Dennison, P.E., & Lundeen, S.R.
664 (2015) Atmospheric correction for global mapping spectroscopy: ATREM advances for
665 the HyspIRI preparatory campaign. *Remote Sensing of Environment, 167*, 64-77
666 Townsend, P.A., Foster, J.R., Chastain, R.A., & Currie, W.S. (2003) Application of imaging
667 spectroscopy to mapping canopy nitrogen in the forests of the central Appalachian
668 Mountains using Hyperion and AVIRIS. *Ieee Transactions on Geoscience and Remote*
669 *Sensing, 41*, 1347-1354
670 Tucker, C.J. (1979) 'Red and Photographic Infrared Linear Combinations for Monitoring
671 Vegetation', *Remote Sensing of Environment*, 8(2), 127-150

672 Ustin, S. L., Gitelson, A. A., Jacquemoud, S., Schaepman, M., Asner, G. P., Gamon, J. A., &
673 Zarco-Tejada, P. (2009) Retrieval of foliar information about plant pigment systems from
674 high resolution spectroscopy. *Remote Sensing of Environment*, *113*, S67-S77
675 Ustin, S.L., & Gamon, J.A. (2010) Remote sensing of plant functional types. *New Phytologist,*
676 *186*, 795-816
677 Vane, G., Green, R.O., Chrien, T.G., Enmark, H.T., Hansen, E.G., & Porter, W.M. (1993) THE
678 AIRBORNE VISIBLE INFRARED IMAGING SPECTROMETER (AVIRIS). *Remote*
679 *Sensing of Environment, 44*, 127-143
680 Vogelmann, J.E., Rock, B.N., & Moss, D.M. (1993) Red edge spectral measurements from sugar
681 maple leaves. *International Journal of Remote Sensing, 14*, 1563-1575
682 Wold, S., Sjöström, M., & Eriksson, L. (2001) PLS-regression: a basic tool of chemometrics.
683 *Chemometrics and Intelligent Laboratory Systems*, 58, 109-130, doi: 10.1016/S0169-
684 7439(01)00155-1
685 Wolter, P.T., Townsend, P.A., Sturtevant, B.R., & Kingdon, C.C. (2008) Remote sensing of the
686 distribution and abundance of host species for spruce budworm in Northern Minnesota
687 and Ontario. *Remote Sensing of Environment, 112*, 3971-3982
688 Xu, K., Metzger, S., & Desai, A.R., (2017). Upscaling tower-observed turbulent exchange at fine
689 spatio- temporal resolution using environmental response functions. *Agricultural and*
690 *Forest Meteorology*, *232*, 10-22, doi:10.1016/j.agrformet.2016.07.019
691 Zarco-Tejada, P.J., Miller, J.R., Noland, T.L., Mohammed, G.H., & Sampson, P.H. (2001)
692 Scaling-up and model inversion methods with narrowband optical indices for chlorophyll
693 content estimation in closed forest canopies with hyperspectral data. *Ieee Transactions on*
694 *Geoscience and Remote Sensing, 39*, 1491-1507

Tables

Table 1. Eddy covariance flux tower site information, including average temperature (°C) and precipitation (%) anomalies for 2013-2014 against the average for 2003 through 2012. SiteID corresponds with Ameriflux Site ID. (PRISM Climate Group, Oregon State University, http://prism.oregonstate.edu, created 17 May 2016)

Site Name	Latitude	Longitude	SiteID	PFT Classification	2013-2014 Temperature anomaly (degrees C)	2013-2014 Precipitation anomaly (percent of average)
Twitchell Island	38.1055	-121.652	USTWT	Wetlands	1.5	61
Twitchell East End Wetland	38.103	-121.641	USTW4	Wetlands	1.8	61
Mayberry Wetland	38.0498	-121.765	USMYB	Wetlands	1.5	63
Tonzi Ranch	38.4316	-120.966	USTon	Grassland-Savanna	1.3	58
Vaira Ranch	38.4067	-120.951	USVar	Grassland-Savanna	1.3	58
Twitchell Alfalfa	38.1159	-121.647	USTW3	Grassland-Savanna	1.5	61
Sherman Island	38.0373	-121.754	USSnd	Grassland-Savanna	1.5	63
Diablo	37.6773	-121.53	USDia	Grassland-Savanna	1.4	63
Oak-Pine Woodland	37.1087	-119.731	USCZ1	Grassland-Savanna	1.5	32
Grassland	33.737	-117.695	USSCg	Grassland-Savanna	1.6	36
Sierran Mixed Conifer Forest	37.0675	-119.195	USCZ3	Forest	1.3	34
Ponderosa Pine Forest	37.0310	-119.257	USCZ2	Forest	1.6	33
Oak-Pine Forest	33.808	-116.772	USSCf	Forest	1.8	51
Coastal Sage	33.734	-117.696	USSCs	Shrubland	1.6	36
Desert Chaparral	33.61	-116.45	USSCc	Shrubland	1.6	46
Pinyon-Juniper Woodland	33.605	-116.455	USSCw	Shrubland	1.6	46
Sky Oaks New	33.38443	-116.64	USSO4	Shrubland	1.5	58
Sky Oaks Young	33.3772	-116.623	USSO3	Shrubland	1.5	58
Sonoran Desert	33.652	-116.372	USSCd	Shrubland	1.5	43

Figures Captions

Figure 1. Location of eddy covariance flux towers (circles) and all AVIRIS flight lines for the study region in 2013 and 2014 (imagery: Google Earth).

Figure 2. Eddy covariance mean daily GPP for each study site, with flight imagery acquisition times noted by dotted lines. Colors represent site plant functional category used in analysis.

Figure 3. Linear Pearson correlation coefficient of tower GPP to airborne imagery spectra normalized difference between all combinations of two bands (NDSI). Black box denotes general region and width of normalized difference vegetation index (NDVI) used by broadband sensors and yellow box the photochemical reflectance index (PRI). This figure includes all sites. Strong positive and negative correlations exist in a number of broad spectral regions. Histogram shows frequency of correlation on legend.

Figure 4. Same as Fig. 3, but based on plant functional category, including a) forests, b) wetlands, c) shrublands, and d) grasslands. In contrast to Fig. 3, many areas of previously significant correlation disappear and those that persist are generally narrower in width.

Figure 5. Predicted 30-minute average GPP (μmol [m^{-2} ground area] s^{-1}) derived by a) partial least squares regression of NDSIs based on all airborne spectra and b) airborne spectra simulated as broadband and applied to a widely used GPP model (Sims *et al.* 2008). While both models capture variability in flux tower GPP across all vegetation types, only the narrowband PLSR model (left) shows low bias and similar performance for all cover types. Bars represent uncertainty in eddy covariance fluxes (vertical, calculated as 20% of the GPP value [Desai *et al.,* 2008]) and PLSR regression (horizontal, calculated as one standard deviation based off the 1000 iterations of the PLSR model).

Figure 6. Coefficients from the PLSR predicting EC-based GPP as a function of NDSIs based on all data pooled across all sites. Values plotted are mean coefficients, based on 1000 permutations, and higher absolute values indicate higher contribution to the predictive model. Only NDSI combinations that were significantly different from zero across the 1000 permutations are plotted. Also shown at bottom (shaded) is histogram of how frequently wavelengths appear in the PLSR predicting EC-based GPP as a function of NDSIs, based on all data pooled across all sites.

730 **Figure 1.** Location of eddy covariance flux towers (circles) and all AVIRIS flight lines for the
731 study region in 2013 and 2014 (imagery: Google Earth).
732

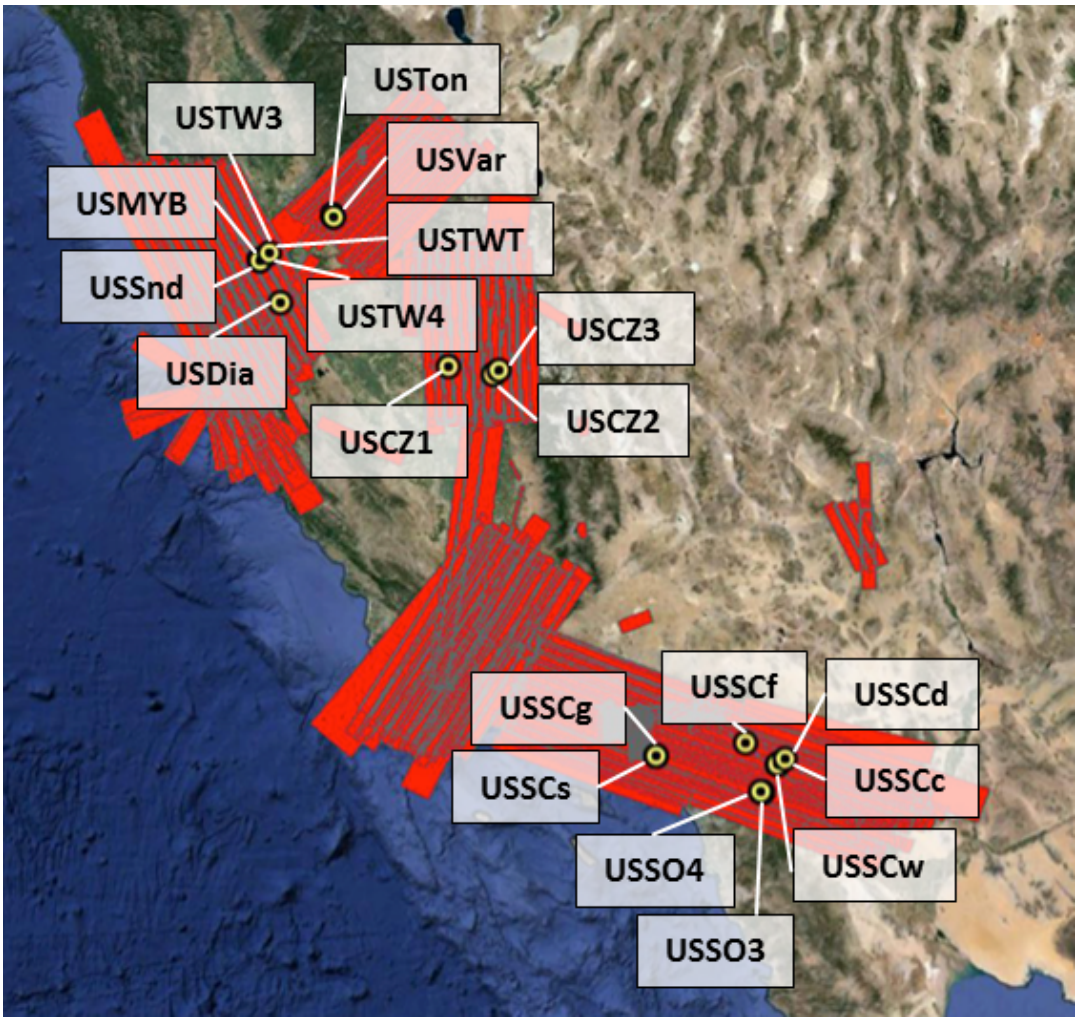

733
734

735 **Figure 2.** Eddy covariance mean daily GPP for each study site, with flight imagery acquisition

736 times noted by dotted lines. Colors represent site plant functional category used in analysis.

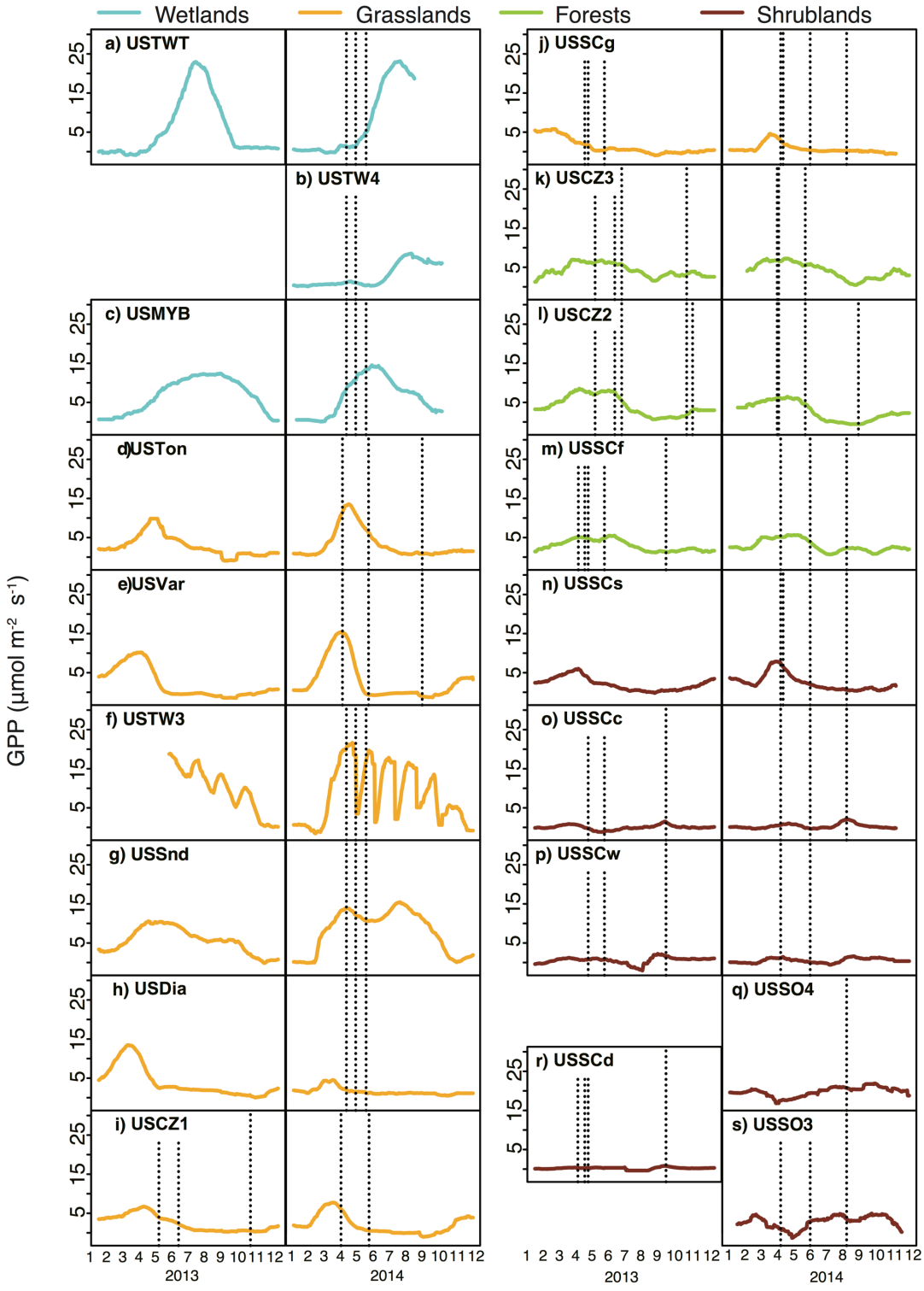

737

738 **Figure 3.** Linear Pearson correlation coefficient of tower GPP to airborne imagery spectra
739 normalized difference between all combinations of two bands (NDSI). Black box denotes
740 general region and width of normalized difference vegetation index (NDVI) used by broadband
741 sensors and yellow box the photochemical reflectance index (PRI). This figure includes all sites.
742 Strong positive and negative correlations exist in a number of broad spectral regions. Histogram
743 shows frequency of correlation on legend.

744

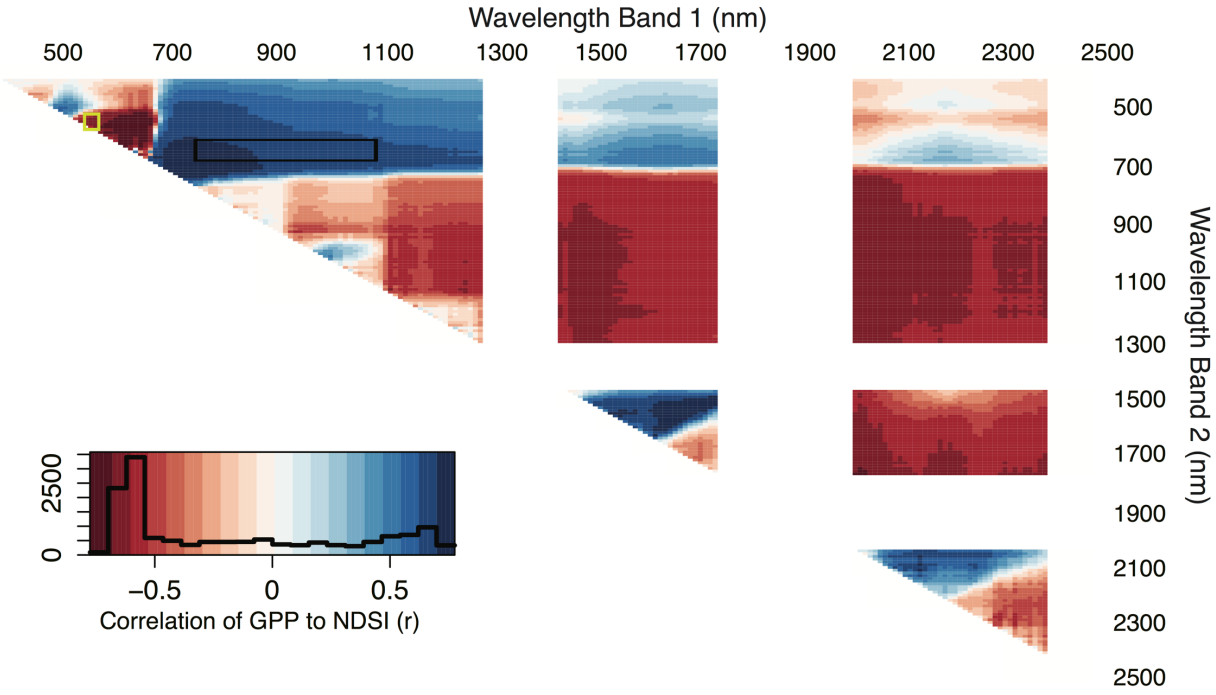

745

Figure 4. Same as Fig. 3, but based on plant functional category, including a) forests, b) wetlands, c) shrublands, and d) grasslands. In contrast to Fig. 3, many areas of previously significant correlation disappear and those that persist are generally narrower in width.

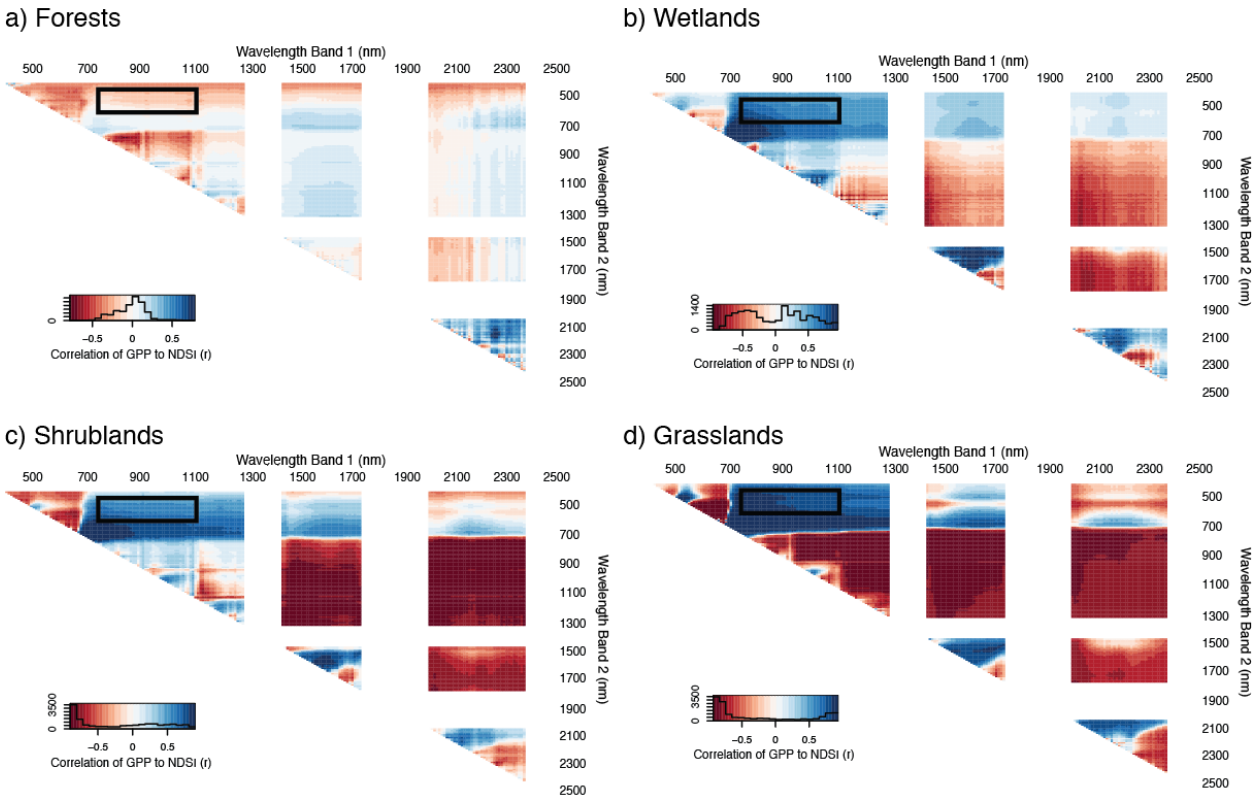

Figure 5. Predicted 30-minute average GPP (µmol [m^{-2} ground area] s^{-1}) derived by a) partial least squares regression of NDSIs based on all airborne spectra and b) airborne spectra simulated as broadband and applied to a widely used GPP model (Sims *et al.* 2008). While both models capture variability in flux tower GPP across all vegetation types, only the narrowband PLSR model (left) shows low bias (validation bias is 0.04 for the PLSR model, and -5.71 for the Sims model) and similar performance for all cover types (Suppl. Table 4). Bars represent uncertainty in eddy covariance fluxes (vertical, calculated as 20% of the GPP value [Desai *et al.,* 2008]) and PLSR regression (horizontal, calculated as one standard deviation based off the 1000 iterations of the PLSR model).

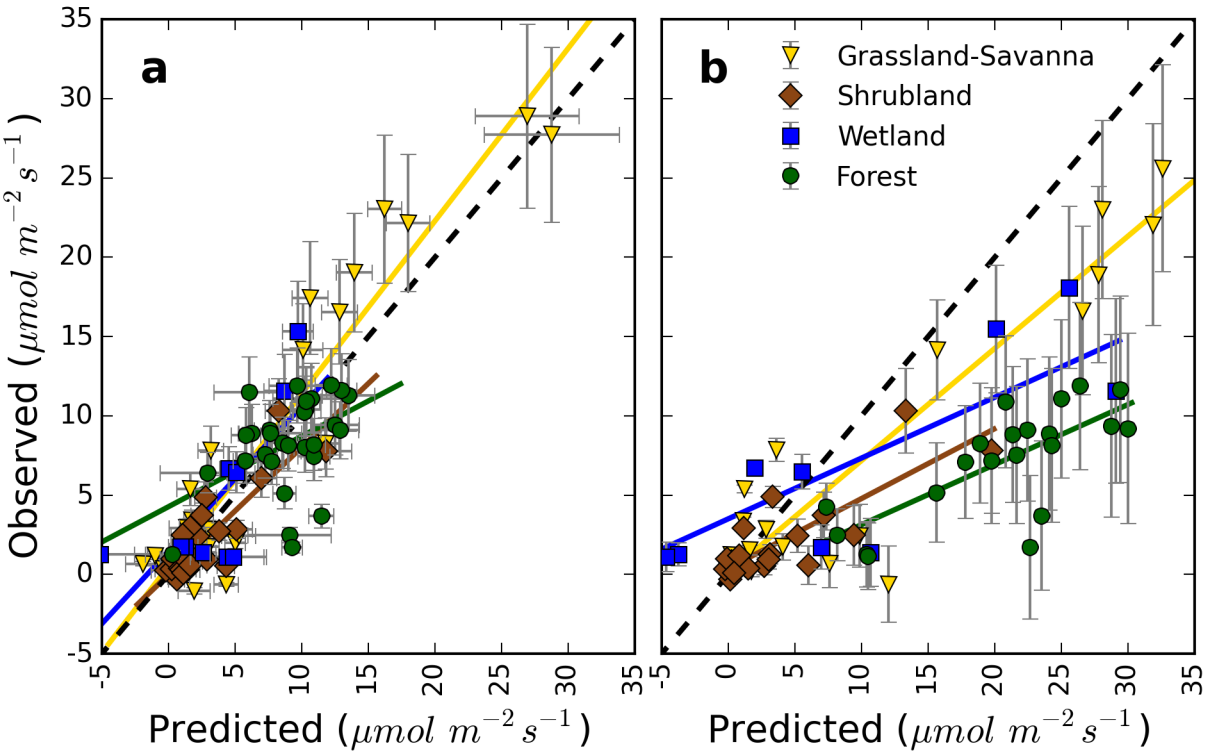

760 **Figure 6.** Coefficients from the PLSR predicting EC-based GPP as a function of NDSIs based on
761 all data pooled across all sites. Values plotted are mean coefficients, based on 1000
762 permutations, and higher absolute values indicate higher contribution to the predictive model.
763 Only NDSI combinations that were significantly different from zero across the 1000
764 permutations are plotted. Also shown at bottom (shaded) is histogram of how frequently
765 wavelengths appear in the PLSR predicting EC-based GPP as a function of NDSIs, based on all
766 data pooled across all sites.

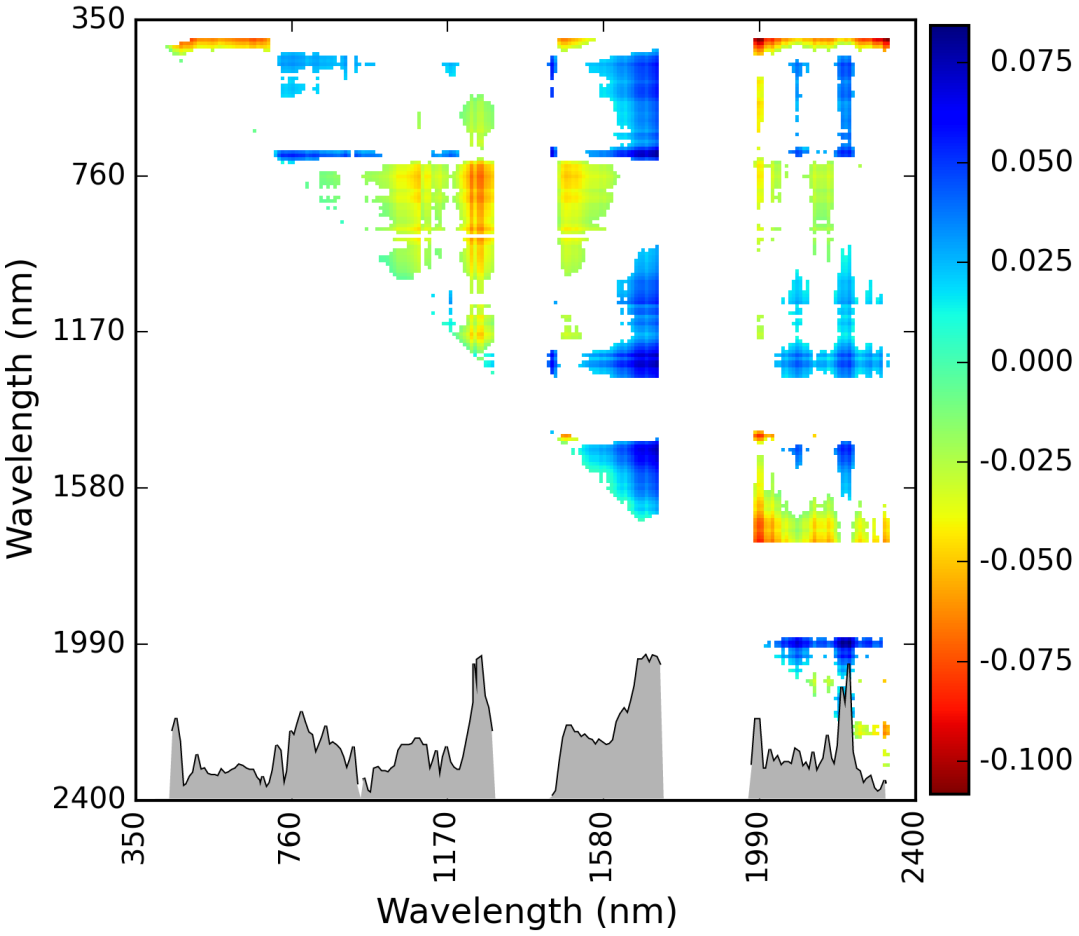

767